Nanoscale

RSC Publishing

PAPER

View Article Online
View Journal | View Issue

Cite this: *Nanoscale*, 2013, **5**, 5093

Single-step solvothermal synthesis of mesoporous Ag–TiO_2–reduced graphene oxide ternary composites with enhanced photocatalytic activity†

Md. Selim Arif Sher Shah,[a] Kan Zhang,[b] A. Reum Park,[a] Kwang Su Kim,[a] Nam-Gyu Park,[a] Jong Hyeok Park[ab] and Pil J. Yoo*[ab]

Received 1st February 2013
Accepted 4th April 2013

DOI: 10.1039/c3nr00579h

www.rsc.org/nanoscale

With growing interest in the photocatalytic performance of TiO_2–graphene composite systems, the ternary phase of TiO_2, graphene, and Ag is expected to exhibit improved photocatalytic characteristics because of the improved recombination rate of photogenerated charge carriers and potential contribution of the generation of localized surface plasmon resonance at Ag sites on a surface of the TiO_2–graphene binary matrix. In this work, Ag–TiO_2–reduced graphene oxide ternary nanocomposites were successfully synthesized by a simple solvothermal process. In a single-step synthetic procedure, the reduction of $AgNO_3$ and graphene oxide and the hydrolysis of titanium tetraisopropoxide were spontaneously performed in a mixed solvent system of ethylene glycol, *N*,*N*-dimethylformamide and a stoichiometric amount of water without resorting to the use of typical reducing agents. The nanocomposites were characterized by X-ray diffraction, X-ray photoelectron spectroscopy, along with different microscopic and spectroscopic techniques, enabling us to confirm the successful reduction of $AgNO_3$ and graphite oxide to metallic Ag and reduced graphene oxide, respectively. Due to the highly facilitated electron transport of well distributed Ag nanoparticles, the synthesized ternary nanocomposite showed enhanced photocatalytic activity for degradation of rhodamine B dye under visible light irradiation.

1 Introduction

The photocatalytic activity of titania has been extensively studied since the discovery of water splitting over titania photoanodes.[1] Titania exhibits several advantageous properties, such as nontoxicity, high photoactivity, photo- and chemical stability, and low production cost, which make it a unique photocatalyst material.[2–5] However, titania has a relatively high band gap energy (~3.2 eV), for which TiO_2 absorbs the radiation only in the UV region, representing 2–4% absorption of the solar spectrum in the lithosphere. Therefore, the photocatalytic activity of TiO_2 can be significantly enhanced if it absorbs light in the visible region (~43% of solar energy), in addition to the small UV fraction. As a result, diverse research activities have focused on shifting the titania band gap to lower values.[6–10] However, expansion into the light absorption region alone cannot necessarily ensure high photocatalytic activity as the separation of the photogenerated electron–hole pairs and their migration to the surface reaction sites also play an important role in determining the photocatalytic performance. Generally, most photogenerated electrons and holes recombine and destroy each other prior to exhibiting the photocatalytic activity as the recombination rates are extremely fast.[11]

In the recent past, graphene, a new class of carbon material comprising single-atom-thick sp^2 hybrid carbon atoms, has received much attention because of its several intriguing characteristics, such as high values of surface area (theoretical value ~2600 $m^2\ g^{-1}$), electron mobility (~15 000 $m^2\ V^{-1}\ s^{-1}$ at room temperature), thermal conductivity, and mechanical strength.[12–17] The unique properties of graphene can be harnessed to form hybrid materials with different metals, metal oxides, chalcogenides and polymers to obtain improved performance in energy and electrochemical applications owing to its improved physicochemical (optical, electrical, mechanical and electrochemical) properties.[16,17] In the case of graphene-hybridized materials, graphene is a potential sink of electrons and can act as a good electron transporting bridge due to its high electron mobility and extended π-electron conjugation, which can stabilize the extraneous electrons.[12–15] This property of graphene plays an important role in decreasing the electron–hole recombination rate, which renders better photocatalytic activity of the graphene composites with metal oxides, particularly with titania, than pure ones. To date, there have been a lot

[a]*School of Chemical Engineering, Sungkyunkwan University, Suwon 440-746, Republic of Korea*

[b]*SKKU Advanced Institute of Nanotechnology (SAINT), Sungkyunkwan University, Suwon 440-746, Republic of Korea. E-mail: pjyoo@skku.edu*

† Electronic supplementary information (ESI) available: XRD of GO, EDX analysis of AgTG composites, tables show the size of graphitic domains and peak area analysis, dye adsorption plot, UV-visible absorption spectra of dye at different times, and plots of $\ln(C_t/C_0)$ *vs.* time with the corresponding fitting curves of different samples. See DOI: 10.1039/c3nr00579h

of reports on titania–graphene composites and their enhanced photocatalytic activity.[18–21] However, there is room to increase the photocatalytic activity of composites either by promoting the light absorption or suppressing the electron–hole recombination rate through incorporating other species into the binary composites.[22]

Noble metal nanoparticles, particularly Ag and Au, have attracted tremendous research interest due to their distinctive optical and catalytic properties.[22–25] These nanoparticles can reduce the recombination rate of the photogenerated electron–hole pairs by transferring the electrons to themselves.[26] Moreover, noble metal nanoparticles may exhibit a localized surface plasmon resonance (LSPR) phenomenon which enables them to have strong and broad absorption in the visible region of the solar spectrum. These factors namely, decrease of recombination rate of the photogenerated charge carriers together with broad absorption of visible light can induce a visible light-driven reaction for photocatalysis in titania.[25,26]

Accordingly, combining Ag and graphene with the ternary nanocomposite photocatalyst of TiO_2 can enhance the photocatalytic performance due to the substantial reduction in the rate of recombination of photogenerated charge carriers by the enhanced electron transport through Ag nanoparticles and graphene. However, current research lacks such studies. For instance, the photocatalytic activity of Ag–TiO_2–graphene has been reported, for which a two-step synthetic route was generally employed.[27,28] The first step involves the solvothermal synthesis of TiO_2–graphene followed by a second step, which involved reduction of silver nitrate by the reducing agent. Similarly, Li *et al.* first synthesized TiO_2–graphene composites on a conducting glass plate by a dipping–lifting process and then formed a Ag–TiO_2–graphene composite using an interfacial reduction reaction with silver nitrate and hydrazine hydrate.[27] However, in these examples of two- or multi-step synthetic routes, pre-formed TiO_2–graphene composites hinder the uniform insertion of Ag nanoparticles, and typically lack to draw the synergistic effect of ternary composite photocatalysts.

In particular, due to their high surface energy, nanoparticles tend to agglomerate particularly in the solid state.[29] Therefore, a multi-step synthetic scheme rarely produces a uniform distribution of the nanoparticles. This challenge can be resolved by introducing a single step experiment. In our previous work, we reported a single step synthesis of TiO_2–reduced graphene oxide (RGO) composites that exhibited good visible light photocatalytic activity.[30] Herein, we report a single-step solvothermal synthesis of Ag–TiO_2–RGO ternary nanocomposites without employing toxic and harsh reducing agents like hydrazine and sodium borohydride. As a result, it is expected that a uniform distribution of TiO_2 and Ag on RGO nanosheets can be readily achieved. Titanium tetraisopropoxide (TIP) was used as a TiO_2 precursor and a mixed solvent system of *N*,*N*-dimethylformamide (DMF) and ethylene glycol (EG) was employed. Notably, DMF alleviates the agglomeration of RGO nanosheets, and EG can induce the reduction of silver nitrate to silver. The as-synthesized ternary composite showed excellent photocatalytic activity towards rhodamine B (RhB) dye degradation under visible light, which outperformed the degradation ability of binary nanocomposites of TiO_2–GRO.

2 Experimental part

Materials

Graphite, TIP, DMF, EG and RhB were obtained from Sigma Aldrich. Potassium permanganate, hydrogen peroxide and ethanol were purchased from Sinopherm Pvt. Ltd. All the chemicals were used as received without further purification. Deionized (DI) water with a resistance of 18.2 MΩ was used. Graphene oxide (GO) was synthesized using a modified Hummers method which is described elsewhere.[30] The synthesized GO was dispersed in DI water by sonication. Indium tin oxide (ITO) substrates for photochemical electrodes were cleaned by sonication in acetone for 30 min, followed by washing with ethanol and DI water.

Synthesis of Ag–TiO_2–RGO nanocomposites

In a typical experiment, 6.0 mL of a GO solution (2.0 mg mL^{-1}) was dried in a rotary evaporator. 25.0 mL DMF was added to the dry product and sonicated for 60 min at room temperature in a bath sonicator. The solution was then centrifuged at 8000 rpm for 8 min. The supernatant was added to a solution of 85.0 mg $AgNO_3$ in 5.0 mL EG and stirred. After 40 min, 0.9 mL TIP was added and stirred for 30 min. DI water of 0.45 mL was added and the mixture was transferred to a 50 mL Teflon liner. The Teflon liner was transferred in a stainless steel autoclave and placed in an oven at 200 °C. The reaction was performed for 18 h and then the autoclave was cooled in an ambient atmosphere naturally. The black precipitate was centrifuged and washed with ethanol several times. The product was then completely dried in an oven at 60 °C. Thus, all the composites contain the same amount of RGO which is ~5 wt% of TiO_2. Hereafter, the synthesized ternary composites of Ag–TiO_2–RGO will be designated as AgTG*x*, where *x* is the moles of metallic Ag. The same procedure was followed to synthesize TiO_2, reduced graphene oxide or a binary composite of TiO_2–RGO that is denoted as TG. Fig. 1 shows the reaction procedure for the solvothermal synthesis of AgTG.

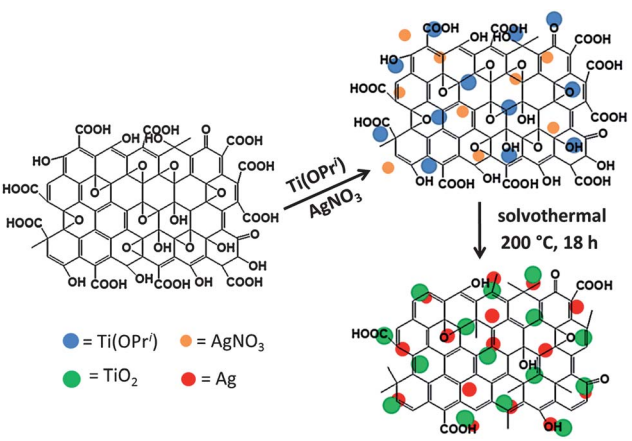

Fig. 1 Synthesis of the ternary composite of AgTG.

Photocatalytic experiment

The photocatalytic dye degradation experiment was followed by measuring the photodegradation of a RhB solution under the illumination of visible light ($\lambda > 400$ nm) at ambient temperature. The experimental procedure was described elsewhere.[30] Briefly, 30 mg of catalyst was dispersed in 50 mL of a 2×10^{-5} M RhB solution under ultrasonication for 2 min. Before illumination, the mixture was magnetically stirred for 45 min in the dark to establish adsorption–desorption equilibrium of the dye with the catalyst. A solar simulator with a Xe lamp (LS-150-Xe, Abet Technologies, Inc., Milford, CT) was used as the visible light ($\lambda > 400$ nm) source. The experimental solution was placed in a quartz cuvette, 100 mm away from the light source. At given intervals, 5 mL of the suspension was withdrawn and centrifuged to remove the dispersed catalyst powder. The concentration of the clean transparent solution was determined by measuring the absorbance of RhB at 553 nm using a spectrophotometer (UV-3600, Shimadzu, Japan).

Photoelectrochemical measurement

A photocurrent measurement experiment was performed in a standard three-electrode system using Pt sheet as the counter electrode, Ag/AgCl (saturated with KCl) as the reference electrode and synthesized catalysts as the working electrodes. A 0.5 M Na_2SO_4 aqueous solution was used as the electrolyte. A portable solar simulator (PEC-L01, Piccell, IRIE Corporation, Japan) was used as the visible light source. Working electrodes were prepared in the following way: a paste of ethyl cellulose (0.06 g) and α-terpineol (0.2 mL) was prepared in ethanol (0.4 mL). Slurry was prepared with the paste and catalyst (0.015 g). The slurry was then coated to a 1×1 cm^2 area of a transparent ITO electrode using the doctor blade technique. The prepared electrodes were then dried in an oven and mildly calcined at 300 °C for 30 min to remove ethyl cellulose and α-terpineol. All the electrodes had similar film thickness (10–15 μm). The photocurrent was measured on an electrochemical analyzer (CHI608C, CH Instruments, Austin, TX).

Characterization

Powder X-ray diffraction (XRD) patterns were obtained (D8 Focus, Bruker instrument, Germany) with Cu Kα radiation ($\lambda =$ 1.5406 Å) in the 2θ range from 3 to 80° with a step size of 0.02° s^{-1}. The accelerating voltage and applied current were 40 kV and 40 mA, respectively. Transmission electron microscopy (TEM, JEM-3010, JEOL, Japan) was performed with an acceleration voltage of 300 kV. FTIR measurements (IFS-66/S, Bruker instrument, Germany) were performed in the transmittance mode in the 400–4000 cm^{-1} spectral range with a resolution greater than 0.1 cm^{-1}. UV-visible absorption spectra were collected from the UV-vis-NIR spectrophotometer (UV-3600, Shimadzu, Japan). Raman spectra were taken using a micro-Raman spectrometer system (ALPHA 300M, WITec, Germany). The sample was loaded on a silica wafer and focused using a 50× objective. The spectra were taken over 1–4000 cm^{-1}. The Brunauer–Emmett–Teller (BET) specific surface areas and porosity of the samples were evaluated on the basis of nitrogen adsorption isotherms measured at 196 °C using a gas adsorption apparatus (ASAP 2020, Micromeritics, Norcross, GA). The samples were degassed at 180 °C before nitrogen adsorption measurements. The BET surface area was determined using adsorption data in the relative pressure (p/p_0) range of 0.06–0.2. X-ray photoelectron spectroscopy (XPS) characterization was performed (ESCA 2000 instrument, VG Microtech, UK) with an Al Kα X-ray source. All binding energy values were corrected by calibrating the C 1s peak at 284.6 eV. High-resolution peaks were deconvoluted using Gaussian–Lorentzian functions with identical full width at half maxima (FWHM) after a Shirley background subtraction.

3 Results and discussion

All the composites contain the same amount of RGO, estimated to be ~5 wt% compared to TiO_2. Fig. 2a depicts the X-ray diffractograms of binary TG and ternary AgTG, indicating that the titania nanoparticles of TG contain both anatase and rutile phases. The TG diffractogram shows peaks at 2θ values of 25.3, 48.0 and 56.0°, which were assigned to the anatase (101), (200) and (211) planes.[30–32] The peaks at 2θ values of 27.3 and 40.1° are assigned to the rutile (110) and (111) planes.[30,32] A separate peak for graphene at a 2θ value of 25° was not observed, which is presumably due to the presence of the anatase (101) peak at 25.3°.[30,32] The diffractogram of AgTG contains all of the anatase and rutile titania peaks mentioned here. Additionally, the peaks at 2θ values of 38.1, 44.4, 64.4 and 77.3° are assigned to the (111), (200), (220) and (311) planes of face centered cubic (FCC) Ag (JCPDS card no. 65-2871).[28,31] This result proves the successful reduction of $AgNO_3$ under the solvothermal

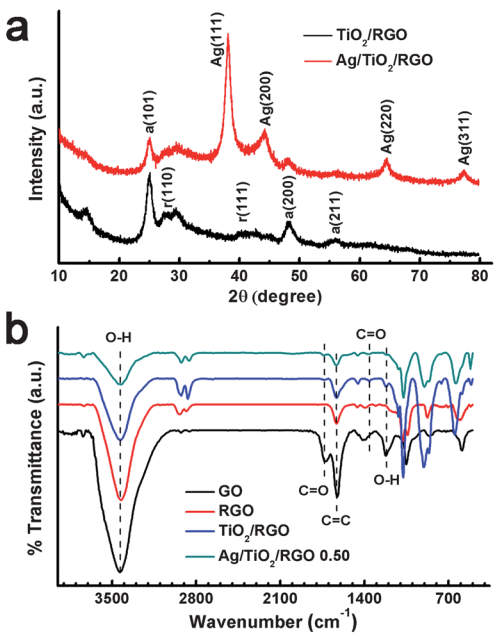

Fig. 2 Crystallographic and chemical functionality analysis of ternary nanocomposites. (a) X-ray diffractogram of TG and AgTG 0.50. The anatase and rutile phases are denoted as 'a' and 'r', respectively. (b) Fourier transform infrared (FT-IR) spectra of GO, RGO, TG and AgTG 0.50.

conditions. The GO diffractogram shown in the ESI (Fig. S1†) exhibits a strong peak at a 2θ value of 10.6°.[30] XRD analysis reveals that titania in the synthesized nanocomposite consists of both anatase and rutile phases. In the reported ternary composites, titania nanoparticles are mostly in a single phase, primarily anatase. However, previous studies showed that mixed phase titania is a better photocatalyst than any one of its single phases.[30,33] Therefore, the composites synthesized here can exhibit good photocatalytic activity. This will be discussed in detail later.

Fig. 2b shows the FTIR spectra of GO, RGO, TG and AgTG. GO exhibits a peak at 1730 cm^{-1} for C=O groups. Peaks at 1228 cm^{-1} and a broad band at ~3430 cm^{-1} are assigned to hydroxyl groups. Carboxyl groups at the edges appear at ~1375 cm^{-1}.[34,35] The FTIR spectrum of RGO reveals that the intensity of the C=O and O–H groups decreased significantly, indicative of the removal of oxygen containing groups after the solvothermal reaction. Peaks at 2854 and 2927 cm^{-1} imply the presence of CH_2 groups in GO. Notably, the intensity of CH_2 increases in RGO, which proves the successful reduction of GO to RGO.[34,35] However, the reduced GO still contains some oxygen containing functionalities, which can induce secondary interactions of RGO with titania and Ag nanoparticles.

In order to evaluate the structural characteristics of the ternary nanocomposites of AgTG, samples were observed with TEM and their surface properties were investigated. Fig. 3a and b show TEM images of a ternary composite of AgTG 0.50. As shown in the figures, Ag and TiO_2 nanoparticles are attached to the graphene layers, wherein the particle diameter is observed to be in the range of 10–25 nm. In particular, these figures show that Ag nanoparticles, darker in color, are stably present over TiO_2 nanoparticles. Fig. 3c shows the high resolution TEM (HRTEM) image of the ternary composite, in which the synthesized nanoparticles of Ag and TiO_2 can be clearly identified by the lattice fringes. Fringe lines with 0.235 nm spacing are for Ag(111) planes and those of 0.315 nm and 0.345 nm are for rutile (110) and anatase (101) planes, respectively.[30,36,37] The presence of Ag and Ti in the ternary nanocomposite can be further confirmed with energy dispersive X-ray (EDX) analysis as presented in Fig. S2.† In addition, a representative nitrogen adsorption–desorption isotherm is shown in Fig. 3d. According to the IUPAC nomenclature, a type IV isotherm with a H1 hysteresis loop is present, which is a typical characteristic of the composite mesoporous structure with cylindrical pore geometry.[30,38]

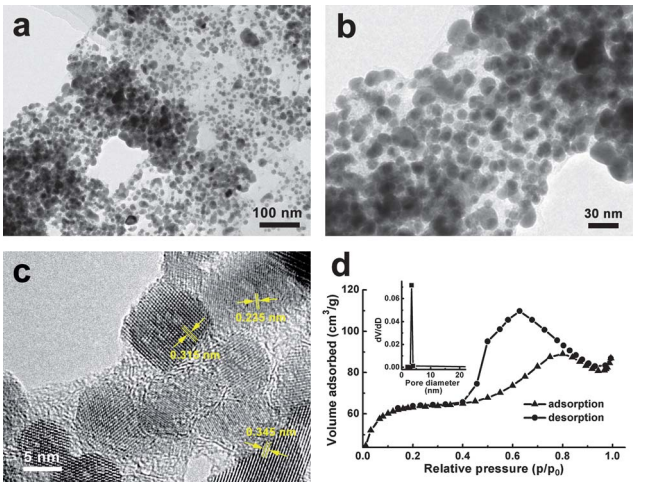

Fig. 3 (a and b) Transmission electron micrographs of AgTG 0.50 with varying magnifications. (c) High resolution TEM (HRTEM) image of AgTG 0.50. (d) Typical nitrogen adsorption–desorption isotherm of AgTG 0.50. The inset corresponds to the pore size distribution measured by the BJH method.

Table 1 shows the parameters obtained from nitrogen desorption isotherms of different samples. It displays that the synthesized samples have a porous structure with a narrow pore size distribution, in the range of 3.0–4.1 nm. Generally, uniformly agglomerated nanoparticles have a narrow distribution of pores in between 1/2 to 1/5 of the primary particle size.[39] The pore sizes of the synthesized materials satisfy this relationship. Therefore, it can be concluded that the synthesized ternary composite comprises densely packed particles which are uniformly agglomerated. This is also manifested from TEM micrographs of the ternary composites. The sample AgTG 0.25 has the highest surface area (347 $m^2\ g^{-1}$). It was attributed to its largest pore volume, 0.37 $cm^3\ g^{-1}$ among all the samples and highly porous structure.[39] With an increasing amount of Ag nanoparticles, the surface area of the ternary composites decreased which was attributed to the decrease of pore volumes. The inset of Fig. 3d represents the pore size distribution of the composite measured by the Barrett–Joyner–Halenda (BJH) method from the desorption branch of the isotherm, revealing a peak centered at ~4.0 nm.

UV-visible absorption spectroscopy analysis was performed to investigate the band edge position of the synthesized materials. Fig. 4a shows the representative spectra of the synthesized materials. The spectra of the ternary composites show greater absorption than those of TiO_2 due to the presence of RGO and Ag nanoparticles in the composites. Moreover, all the ternary composites show a broad absorption peak at approximately 390 nm, which can be attributed to the surface plasmon resonance of Ag nanoparticles.[40] The position of the plasmon peak indicates that the average size of the Ag nanoparticles is 10–20 nm, which matches well with the results from the TEM analysis.[40] Moreover, the obtained UV-visible spectra clearly show that the band edge of the ternary composite shifts towards

Table 1 Parameters obtained from the nitrogen desorption isotherm experiments

Sample	Mean pore size[a] (nm)	Pore volume[b] ($cm^3\ g^{-1}$)	Surface area[c] ($m^2\ g^{-1}$)
P25[d]	27.9	0.13	39
TG	3.0	0.12	324
AgTG 0.25	3.6	0.37	347
AgTG 0.50	4.0	0.06	215
AgTG 0.75	4.1	0.08	176

[a] Average pore diameter was estimated from the BJH formula. [b] BJH desorption cumulative pore volume between 1.7 and 300.0 nm diameter. [c] BET specific surface area was calculated from the linear part of the corresponding BET plot. [d] Ref. 30.

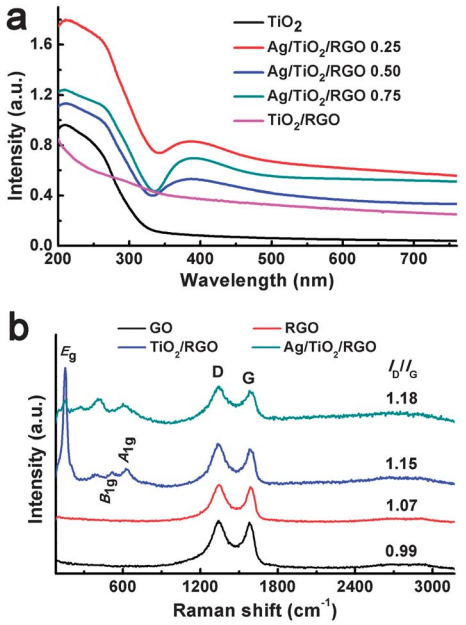

Fig. 4 (a) UV-visible absorption spectra of TiO_2 and AgTG with different concentrations of Ag nanoparticles. (b) Raman spectra of GO, RGO, TG and AgTG 0.50.

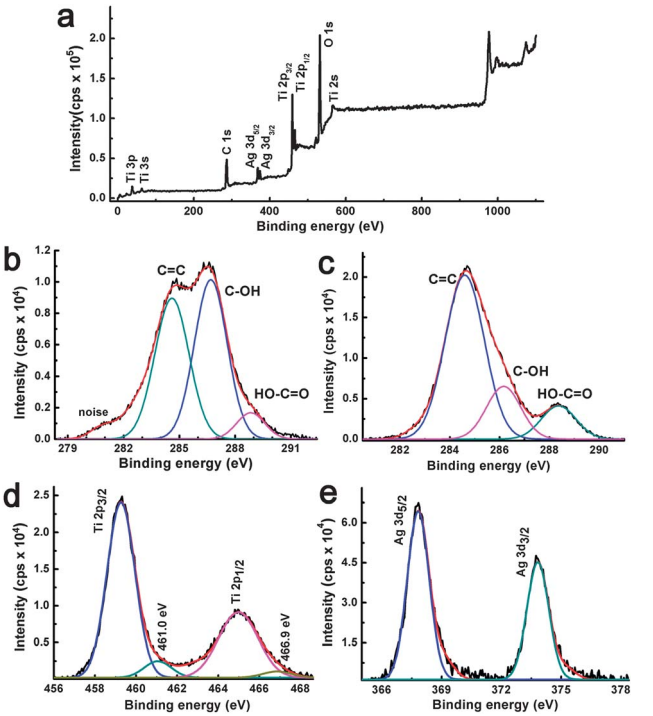

Fig. 5 (a) Survey XPS spectrum of AgTG 0.25. (b) Core level C 1s spectra of GO. Core level XPS spectra of (c) C 1s, (d) Ti 2p and (e) Ag 3d of AgTG 0.25.

the visible region compared to that of the as-synthesized TiO_2. Therefore, the composites can have a good photocatalytic activity, exceeding TiO_2. For comparison, the UV-visible spectrum of the binary composite of TG is also depicted, wherein no absorption peaks were observed near 390 nm.

Fig. 4b depicts the Raman spectra of GO, RGO, TG and AgTG. The Raman spectrum of GO shows D- and G-bands at ~1342 and ~1583 cm^{-1}, respectively.[41] The D-band corresponds to the disorder band associated with structural defects created in graphene (RGO) during the reduction of GO. On the other hand, the G-band corresponds to the first order scattering of the E_{2g} phonon of sp^2 C atoms of graphene. The intensity ratio of these two bands was 0.99. The D- and G-bands of RGO, TG and AgTG were roughly at the similar position to those of GO. However, the I_D/I_G ratio of RGO increased to 1.07 from 0.99 for GO, which proves the reduction of GO during the solvothermal experiment. The I_D/I_G ratio (1.15) of the binary composite was greater than that of RGO. This observation implies that smaller domains of GO were created in the presence of TiO_2, as compared to the synthesis of RGO under the same experimental conditions.[41] The Raman spectrum of the composite TG shows peaks at 157, 401 and 517 cm^{-1}, which were assigned to E_g, B_{1g} and A_{1g} of anatase titania, respectively, whereas the peaks at 157 and 630 cm^{-1} were attributed to B_{1g} and A_{1g} of rutile titania. Therefore, the Raman spectra further proved that the synthesized titania was composed of both anatase and rutile phases.[30,42] The Raman spectrum of the ternary composite AgTG showed that the I_D/I_G ratio further increased to 1.18, which indicates more of a decrease of graphitic domains. The rutile and anatase peaks present in the binary composite, all exist in the ternary composite. Each spectrum shows very weak 2D and S3 peaks as well. Table S1† shows the graphitic domain size of all the samples.

Fig. 5a represents a XPS survey spectrum of the AgTG composite, demonstrating that the composite contains Ag, Ti, O and C. Chemical binding energies are observed at 367.8, 458.3, 529.6 and 284.5 eV for Ag $3d_{5/2}$, Ti $2p_{3/2}$, O 1s and C 1s, respectively. The survey XPS spectrum does not have a peak at ~400 eV, indicating the absence of the nitrogen.[43] Fig. 5b shows the C 1s XPS spectrum of GO. The peak at 284.5 eV is assigned to the sp^2 carbon atoms of GO. Peaks at higher binding energies are assigned to the oxygenated carbon species of GO, such as C–OH, C═O, COOH, *etc.*[30,44] Fig. 5c depicts the C 1s XPS spectrum of the AgTG nanocomposite, illustrating the significantly decreased peak intensities of the oxygenated carbon species at 286–289 eV after solvothermal reaction. This observation implies that GO was substantially reduced after the solvothermal reaction to form RGO while still containing some oxygenated groups. This is also verified from Table S2,† indicating that over 50% removal of oxygen containing groups takes place in the ternary composite during a reduction from GO to RGO. The presence of oxygenated groups in RGO has been also identified from the FTIR analysis. The oxygenated groups in RGO can serve as interaction sites with TiO_2 nanoparticles. The representative Ti core level XPS spectrum depicted in Fig. 5d indicates two peaks centered at 459.26 and 464.97 eV, assigned to Ti $2p_{3/2}$ and Ti $2p_{1/2}$, respectively. The splitting between these two bands was ~5.7 eV. These observations confirm that in the composites Ti exists mainly in the Ti^{4+} state.[30,44] Moreover, this spectrum shows two weak peaks centered at 461.0 and 466.9 eV. These peaks may be due to the formation of a higher valence state, Ti^{5+} of the type Ti_2O_5.[45] Fig. 5e shows a representative Ag 3d core level XPS spectrum with two peaks centered at 367.8 and

373.8 eV for Ag $3d_{5/2}$ and Ag $3d_{3/2}$, respectively, with 6 eV splitting between two peaks that is evidence of the reduction of $AgNO_3$ by the solvothermal method to produce metallic silver.[31] Here it needs to be mentioned that the RGO was further reduced during the photocatalytic dye degradation experiment and eventually some RGO was degraded (please see Table S2† and the explanation therein).

Photoelectrochemical properties of the ternary composites were characterized by measuring the photocurrent. The mild calcination conditions of the electrodes at 300 °C for 30 min were chosen not to significantly affect the properties of the composites.[46] The potential of the working electrode was maintained at 1.2 V against the Pt counter electrode (1×1 cm^2). Fig. 6a shows the photocurrent response of the composites together with P25 commercial TiO_2 nanoparticles. The as-synthesized TiO_2 exhibits a photocurrent of ~2.8 μA, whereas the binary composite of TG (TiO_2–RGO) showed a photocurrent value of 3.1 μA. Notably, the ternary composites of AgTG 0.25 showed almost two times enhanced photocurrent values compared to those of the synthesized TiO_2. The reasons behind this excellent electrochemical property of AgTG composites are that graphene (RGO) has outstanding electron mobility and can also act as an electron sink.[12–15] Therefore, the photogenerated electrons in the composites can be accepted and promptly transported by graphene, which eventually leads to a decrease of the recombination rate of electron–hole pairs. Simultaneously, the photogenerated electrons can be captured and transported by Ag nanoparticles. Additionally, due to the occurrence in surface plasmon resonance, the interfacial electron transfer is highly facilitated by Ag nanoparticles. As a result, the ternary composites produced a high photocurrent under visible light irradiation. Whereas, under the same conditions, P25 nanoparticles showed a photocurrent value of 2.9 μA.

Fig. 6b demonstrates the representative photoluminescence (PL) spectra of the as-synthesized TiO_2, TG and AgTG composites. The intensity of the PL spectrum is a direct measurement of the electron–hole recombination rate, *i.e.* the faster the recombination occurs, the more intense the spectrum is. Alternatively, a lower intensity indicates that more excited electrons are trapped and stably transferred through the interface. The two emission bands in the PL spectra of TiO_2 at ~363 and ~394 eV are due to the direct and indirect transitions of TiO_2, respectively.[39] The emission signals at ~422 and ~446 nm are attributed to the excitonic PL peaks trapped by defects and surface states.[47] The band at ~486 nm may be due to the charge transfer transition from Ti^{3+} to oxygen vacancies at the surface.[48] The existence of Ti^{3+} species was not clear from the XPS spectra, possibly due to the low concentration of Ti^{3+} species. However, the presence of such species cannot be excluded for TiO_2 as it is a reducible oxide and Ti is highly reactive towards oxygen.[49] These two causes led to the formation of different Ti oxides with different stoichiometries, the existence of which is more difficult to identify with XPS. The peak at ~545 nm may be due to the Ti site vacancies created in TiO_2.[50] After the formation of the binary composite of TG, the PL intensity of TiO_2 decreased markedly and some of the above mentioned bands disappeared. This change is attributed to the trapping of the photo-excited electrons by RGO. In the ternary composite, the PL intensity decreased further. It was attributed to the existence of Schottky barriers at the interface of Ag and TiO_2 which can serve as an electron trap, preventing electron–hole recombination.[51] A comparative study of PL data and the photoelectrochemical experiments reveals that the obtained results are consistent with each other.

The synthesized AgTG composites were applied for a photocatalytic degradation of RhB dye under visible light (>400 nm) exposure at room temperature and pressure. Prior to irradiation, the mixture of the dye and catalyst was stored in the dark to attain adsorption–desorption equilibrium (see the Experimental part). The amount of adsorbed dye was measured by UV-visible spectroscopy and plotted against the catalyst (Fig. S3†). We did not observe any obvious correlation between the amounts of dye adsorbed with the surface area of different composites (compare Table 1 and Fig. S3 in ESI†). This may be due to the presence of the same amount of graphene (~5 wt% of TiO_2) in all samples. However, for the ternary composites, the amount of adsorbed dye increased slightly with increasing the surface area of the composites. Fig. 7a shows the normalized concentration against the time for different reaction mixtures. Under the non-catalyst (only RhB) or graphene-only conditions, the degradation of RhB after 60 min of visible light exposure is negligible, as shown in (1) and (2). This indicates that RhB neither self-degrades nor can it be degraded by graphene under visible light exposure. Under the same conditions, P25 can degrade ~20% of the dye (3), while the as-synthesized TiO_2 can

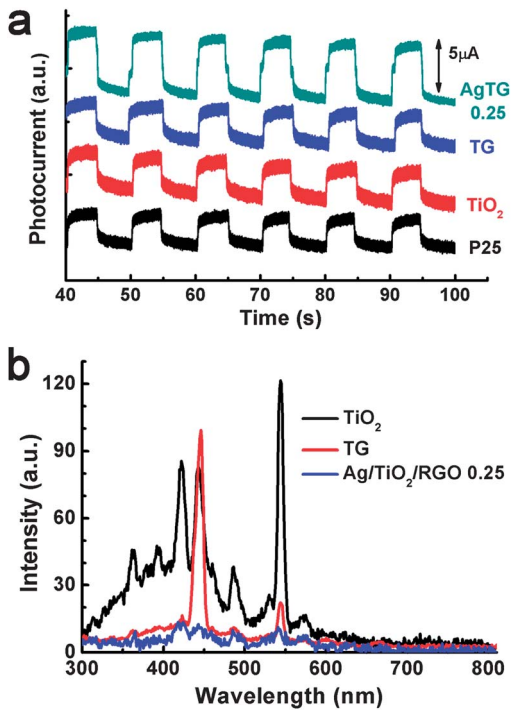

Fig. 6 (a) Plot of photocurrent *vs.* time for P25, as-synthesized TiO_2, TG and AgTG 0.25. (b) Photoluminescence spectra of the as-synthesized TiO_2, binary composite TG and ternary composite AgTG 0.25.

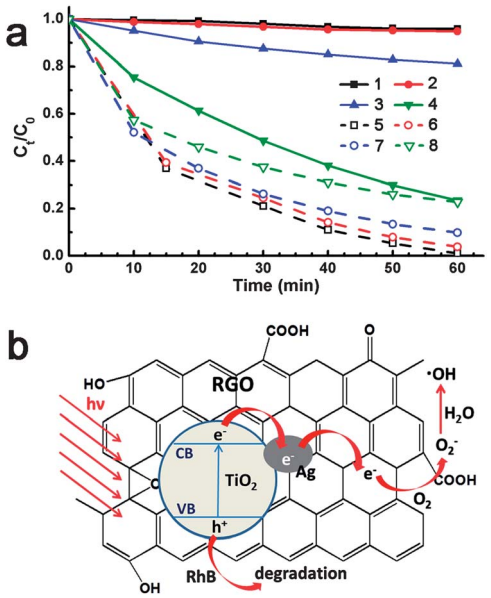

Fig. 7 (a) Plot showing the concentration change of RhB dye at different times during the photocatalytic degradation experiment (1) without catalyst and with (2) RGO, (3) P25, (4) TG, (5) AgTG 0.10, (6) AgTG 0.25, (7) AgTG 0.50 and (8) AgTG 0.75. (b) Pathways of electron transfer and mechanism of the degradation of RhB dye.

degrade only ~15% of the dye (not shown). However, the photocatalytic activity of the as-synthesized TiO_2 is significantly enhanced in the presence of graphene, particularly with the coexistence of Ag and graphene. The curves show that the best photocatalytic activity is achieved by the composite AgTG 0.10. However, with a further increase or decrease (for AgTG 0.05, not shown in figure, in which ~93% RhB was degraded after 60 min of visible light exposure) in the concentration of Ag in the composites, the photocatalytic activity gradually decreased as shown in the curves (6), (7), and (8).

The bar plot in Fig. S3 (ESI†) shows that the amounts of dye adsorbed by AgTG 0.10, AgTG 0.25, AgTG 0.50 and AgTG 0.75 were comparable (56–60%). Therefore, the amount of adsorbed dye negligibly affects the decreased photocatalytic activity with an increased amount of Ag in the composite. However, with an increased amount of Ag, some of the active sites of the catalysts in the ternary composites can be undesirably occupied by the Ag nanoparticles, resulting in decreased photocatalytic activity. For comparison, the photocatalytic activity of TG is also shown in (4). Except for the case of AgTG 0.75, all the ternary composites are photocatalytically more active than the TiO_2–graphene composites. This experimental observation verifies our assumption that the inclusion of Ag nanoparticles in the TiO_2–graphene composite can substantially increase its photocatalytic activity. The UV-visible spectra of the dye at different time intervals are shown in Fig. S4.† The kinetic data of photocatalytic degradation were fitted by a pseudo-first order reaction. The rate constants (last points were not considered) were 0.004, 0.024, 0.056, 0.048, 0.032, and 0.022 min^{-1} for P25, TG, AgTG 0.10, AgTG 0.25, AgTG 0.50 and AgTG 0.75, respectively. The data reveal that the AgTG 0.10 catalyst shows better efficiency by an order of magnitude for the photocatalytic degradation of RhB than that of P25. Fitting curves for the determination of rate constants are shown in Fig S5.†

As discussed earlier and depicted in Fig. 7a, it is obvious that the ternary composite exhibits a marked enhancement in the photocatalytic activity of RhB under visible light irradiation compared to the as-synthesized TiO_2. As a relevant reaction mechanism, therefore, the following scenario can be proposed. Generally, titania exists in different oxides and contains a lot of defects, particularly due to heterojunctions that decrease the energy of its conduction band as much as 1 eV.[30,49,52] Therefore, it is possible that such types of titania can absorb visible light to promote electrons from the valence band to the conduction band. These electrons can then be transferred to the Ag clusters that are deposited on TiO_2, and subsequently to RGO. As a result, the electron–hole pair recombination rate can be decreased, which is schematically depicted in Fig. 7b. Eventually, these electrons reduce the dissolved oxygen, leading to the formation of reduced O_2^- ions. Several studies proposed that the formation of O_2^- *via* reduction of O_2 by the photogenerated electrons is the slowest step in the course of photocatalytic reaction pathways.[30,53,54] Thus, the surface deposited Ag nanoparticles can increase the rate of formation of O_2^- while simultaneously decreasing the rate of recombination.[47] In the final state, the reaction of O_2^- with H_2O forms ·OH radicals, which degrade the RhB dye. In parallel, the holes on the valence band can break apart water molecules to form hydroxyl radicals and/or degrade the dye directly. Following are the reactions that occurred for the dye degradation.

$$e^- + O_2 \rightarrow O_2^-$$

$$O_2^- + H_2O \rightarrow {}^{\cdot}OH$$

$$^{\cdot}OH + RhB \rightarrow \text{Degradation of RhB}$$

4 Conclusions

A series of ternary composites of Ag–TiO_2–reduced graphene oxide has been successfully synthesized by a single step solvothermal reaction while excluding the use of conventional harsh reducing agents. The composites were well characterized by different instrumental techniques and the results were correlated. The titania nanoparticles in the composites are present in both anatase and rutile phases. The uniformly distributed Ag and TiO_2 nanoparticles less than 25 nm in diameter were confirmed by TEM observation. UV-visible absorption spectroscopy shows the presence of a surface plasmon peak for Ag nanoparticles at ~390 nm. For an application, the synthesized composites were demonstrated with efficient catalysis towards the degradation of RhB dye under visible light irradiation. As a result, over 99% of the dye was degraded by the catalyst AgTG 0.10. The degradation of the dye follows pseudo-first order kinetics. The composite AgTG 0.10 showed a significantly increased rate constant, as compared to that of the commercial TiO_2, P25. Therefore, the presented ternary composite is potentially useful for a catalyst for solar water splitting.

Acknowledgements

This work was supported by research grants of NRF (2012M1A2A2671795), Global Frontier R&D Program on Center for Multiscale Energy System (2012M3A6A7055540), and Basic Science Research Program (2012-0009158) funded by the National Research Foundation under the Ministry of Science, ICT & Future, Korea. This research was also supported by a grant (10037872) from the Fundamental R&D Program for Technology of World Premier Materials funded by the Ministry of Knowledge Economy (MKE) of Korea.

References

1 A. Fujishima and K. Honda, *Nature*, 1972, **238**, 37–38.
2 M. Niederberger, M. H. Bartl and G. D. Stucky, *Chem. Mater.*, 2002, **14**, 4364–4370.
3 M. S. Wong, E. S. Jeng and J. Y. Ying, *Nano Lett.*, 2001, **1**, 637–642.
4 J. Fan, L. Zhao, J. Yu and G. Liu, *Nanoscale*, 2012, **4**, 6597–6603.
5 J. Polleux, N. Pinna, M. Antonietti, C. Hess, U. Wild, R. Schlçgl and M. Niederberger, *Chem.–Eur. J.*, 2005, **11**, 3541–3551.
6 S. U. M. Khan, M. Al-Shahry and W. B. Ingler, *Science*, 2002, **297**, 2243–2245.
7 J. Graciani, L. J. Alvarez, J. A. Rodriguez and J. F. Sanz, *J. Phys. Chem. C*, 2008, **112**, 2624–2631.
8 V. Subramanian, E. E. Wolf and P. V. Kamat, *J. Am. Chem. Soc.*, 2004, **126**, 4943–4950.
9 S. H. Elder, F. M. Cot, Y. Su, S. M. Heald, A. M. Tyrysgkin, M. K. Bowman, Y. Gao, A. G. Joly, M. L. Balmer, A. C. Kolwaite, K. A. Magrini and D. M. Blake, *J. Am. Chem. Soc.*, 2000, **122**, 5138–5146.
10 X. Chen, L. Liu, P. Y. Yu and S. Mao, *Science*, 2011, **331**, 746–750.
11 K. Zhou, Y. Zhu, X. Yang, X. Jiang and C. Li, *New J. Chem.*, 2011, **35**, 353–359.
12 X. Y. Zhang, H. P. Li, X. L. Cui and Y. Lin, *J. Mater. Chem.*, 2010, **20**, 2801–2806.
13 N. Zhang, Y. Zhang and Y. J. Xu, *Nanoscale*, 2012, **4**, 5792–5813.
14 F. Schedin, A. K. Geim, S. V. Morozov, E. M. Hill, P. Blake, M. I. Katsnelson and K. S. Novoselov, *Nat. Mater.*, 2007, **6**, 652–655.
15 S. Watcharotone, D. A. Dikin, S. Stankovich, R. Piner, I. Jung, G. H. B. Mommett, G. Evmenenko, S. E. Wu, S. F. Chen and C. P. Liu, *Nano Lett.*, 2007, **7**, 1888–1892.
16 T. Takamura, K. Endo, L. Fu, Y. P. Wu, K. J. Lee and T. Matsumoto, *Electrochim. Acta*, 2007, **53**, 1055–1061.
17 N. Zhang, Y. Zhang, X. Pan, M. Q. Yang and Y. J. Xu, *J. Phys Chem C*, 2012, **116**, 18023–18031.
18 J. Zhang, Z. Xiong and X. S. Zhao, *J. Mater. Chem.*, 2011, **21**, 3634–3640.
19 L. Sun, Z. Zhao, Y. Zhou and L. Liu, *Nanoscale*, 2012, **4**, 613–620.
20 O. Akhavan and E. Ghaderi, *J. Phys. Chem. C*, 2009, **113**, 20214–20220.
21 P. V. Kamat, *J. Phys. Chem. Lett.*, 2011, **2**, 242–251.
22 T. Nguyen, C. T. Dinh and T. O. Do, *Nanoscale*, 2011, **3**, 1861–1873.
23 A. Furube, L. Du, K. Hara, R. Katoh and M. Tachiya, *J. Am. Chem. Soc.*, 2007, **129**, 14852–14853.
24 S. Naya, A. Inoue and H. Tada, *J. Am. Chem. Soc.*, 2010, **132**, 6292–6293.
25 Q. Zhang, D. Q. Lima, I. Lee, F. Zaera, M. Chi and Y. Yin, *Angew. Chem., Int. Ed.*, 2011, **50**, 7088–7092.
26 P. D. Cozzoli, R. Comparelli, E. Fanizza, M. L. Curri, A. Agostiano and D. Laub, *J. Am. Chem. Soc.*, 2004, **126**, 3868–3879.
27 G. Li, T. Wang, Y. Zhu, S. Zhang, C. Mao, J. Wu, B. Jin and Y. Tian, *Appl. Surf. Sci.*, 2011, **257**, 6568–6572.
28 Y. Wen, H. Ding and Y. Shan, *Nanoscale*, 2011, **3**, 4411–4417.
29 K. Shankar, J. I. Basham, N. K. Allam, O. K. Varghese, G. K. Mor, X. Feng, M. Paulose, J. A. Seabold, K. S. Choi and C. A. Grimes, *J. Phys. Chem. C*, 2009, **113**, 6327–6359.
30 M. S. A. Sher Shah, A. R. Park, K. Zhang, J. H. Park and P. J. Yoo, *ACS Appl. Mater. Interfaces*, 2012, **4**, 2107–2115.
31 M. S. A. Sher Shah, M. Nag, T. Kalagara, S. Singh and S. V. Manorama, *Chem. Mater.*, 2008, **20**, 2455–2460.
32 Y. Zhang, Z. R. Tang, X. Fu and Y. J. Xu, *ACS Nano*, 2011, **5**, 7426–7435.
33 S. Cong and Y. Xu, *J. Phys. Chem. C*, 2011, **115**, 21161–21168.
34 C. Nethravathi and M. Rajamathi, *Carbon*, 2008, **46**, 1994–1998.
35 J. S. Park, S. M. Cho, W. J. Kim, J. Park and P. J. Yoo, *ACS Appl. Mater. Interfaces*, 2011, **3**, 360–368.
36 S. George, S. Lin, Z. Ji, C. R. Thomas, L. J. Li, M. Mecklenburg, H. Meng, X. Wang, H. Zhang, T. Xia, J. N. Hohman, S. Lin, J. I. Zink, P. S. Weiss and A. E. Nel, *ACS Nano*, 2012, **6**, 3745–3759.
37 K. Thamaphat, P. Limsuwan and B. Ngotawornchai, *Kasetsart J.: Nat. Sci.*, 2008, **42**, 357–361.
38 L. Sun, Z. Zhao, Y. Zhou and L. Liu, *Nanoscale*, 2012, **4**, 613–620.
39 N. Lakshminarasimhan, E. Bae and W. Choi, *J. Phys. Chem. C*, 2007, **111**, 15244–15250.
40 J. Li and C.-Y. Liu, *Eur. J. Inorg. Chem.*, 2010, **8**, 1244–1248.
41 J. Gao, F. Liu, Y. Liu, N. Ma, Z. Wang and X. Zhang, *Chem. Mater.*, 2010, **22**, 2213–2218.
42 V. Swamy, B. C. Muddle and Q. Dai, *Appl. Phys. Lett.*, 2006, **89**, 163118.
43 Y. Wang, Y. Shao, D. W. Matson, J. Li and Y. Lin, *ACS Nano*, 2010, **4**, 1790–1798.
44 O. Akhavan, M. Abdolahad, A. Esfandiar and M. Mohatashamifar, *J. Phys. Chem. C*, 2010, **114**, 12955–12959.
45 T. Abe, E. Suzuki, K. Nagoshi, K. Miyashita and M. Kaneko, *J. Phys. Chem. B*, 1999, **103**, 1119–1123.
46 W. Xie, Y. Li, W. Sun, J. Huang, H. Xie and X. Zhao, *J. Photochem. Photobiol., A*, 2010, **216**, 149–155.
47 B. Liu, L. Wen and X. Zhao, *Mater. Chem. Phys.*, 2007, **106**, 350–353.
48 J. Liu, J. Li, A. Sedhain, J. Lin and H. Jiang, *J. Phys. Chem. C*, 2008, **112**, 17127–17132.

49 U. Diebold and T. E. Madey, *Surf. Sci. Spectra*, 1998, **4**, 227–231.
50 T. Sasaki and M. Watanable, *J. Phys. Chem. B*, 1997, **101**, 10159–10161.
51 J. Shi, J. Chen, Z. Feng, T. Chen, Y. Lian, X. Wang and C. Li, *J. Phys. Chem. C*, 2007, **111**, 693–699.
52 J. Strunk, W. C. Vining and A. T. Bell, *J. Phys. Chem. C*, 2010, **114**, 16937–16945.
53 R. Wang, G. Jiang, Y. Ding, Y. Wang, X. Sun, X. Wang and W. Chen, *ACS Appl. Mater. Interfaces*, 2011, **3**, 4154–4158.
54 F. Petronella, E. Fanizza, G. Mascolo, V. Locaputo, L. Bertinetti, G. Martra, S. Coluccia, A. Agostiano, M. L. Curri and R. Comparelli, *J. Phys. Chem. C*, 2011, **115**, 12033–12040.